

Plasma flow versus magnetic feature-tracking speeds in the Sun

G. Guerrero,^{1*} M. Rheinhardt,¹ A. Brandenburg^{1,2} and M. Dikpati³

¹*NORDITA, AlbaNova University Center, Roslagstullsbacken 23, SE-10691 Stockholm, Sweden*

²*Department of Astronomy, AlbaNova University Center, Stockholm University, SE-10691 Stockholm, Sweden*

³*High Altitude Observatory, National Center for Atmospheric Research, 3080 Center Green, Boulder, CO 80301, USA*

Accepted 2011 September 30. Received 2011 September 28; in original form 2011 July 24

ABSTRACT

We simulate the magnetic feature-tracking (MFT) speed using axisymmetric advective–diffusive transport models in both one and two dimensions. By depositing magnetic bipolar regions at different latitudes at the Sun’s surface and following their evolution for a prescribed meridional circulation and magnetic diffusivity profiles, we derive the MFT speed as a function of latitude. We find that in a one-dimensional surface-transport model the simulated MFT speed at the surface is always the same as the meridional flow speed used as input to the model, but is different in a two-dimensional transport model in the meridional (r, θ) plane. The difference depends on the value of the magnetic diffusivity and on the radial gradient of the latitudinal velocity. We have confirmed our results with two different codes in spherical and Cartesian coordinates.

Key words: convection – magnetic fields – MHD – Sun: activity – surface magnetism.

1 INTRODUCTION

At the solar surface, magnetic features are, apart from active regions and sunspots, observed in the form of small magnetic elements of both polarities which appear at all latitudes. Tracking the motion of such a structure individually, one finds in general a poleward migration which is suggestive of a poleward meridional flow at and just beneath the Sun’s surface. However, Doppler measurements¹ of the poleward flow speed at the surface reveal a systematic difference from the speed inferred from magnetic feature tracking (MFT): at low and mid latitudes, the latter is observed to be lower than the Doppler speed, but similar to it at high latitudes (see fig. 10 of Ulrich 2010). Sunspots are usually discarded in such an analysis (Komm, Howard & Harvey 1993; Hathaway & Rightmire 2010) because their motion may be affected by their strong magnetic fields. To understand the physical origin of these differences, Dikpati, Gilman & Ulrich (2010) performed a simple test using a two-dimensional (axisymmetric) advective–diffusive flux-transport model. They showed in simulations that, due to diffusive transport, the MFT speed can indeed be different from that of the meridional flow fed into the model. They attributed this difference to the latitudinal gradient of the radial component of the magnetic field, directed towards the equator at the equatorward side of a bipolar region and towards the pole at its poleward side. They concluded that magnetic features

drift polewards with a net speed that is lower than the flow speed at low latitudes and higher at high latitudes.

In non-axisymmetric two-dimensional (θ, ϕ) surface-transport models (e.g. Baumann et al. 2004; Wang, Robbrecht & Sheeley 2009; Sheeley 2010), one could likewise suppose that diffusion is the only agent that can prevent magnetic features from simply being advected with the meridional flow. However, a difference between Doppler and MFT speeds has never been discussed for those models.

In this Letter, we use both one-dimensional (latitudinal) and two-dimensional (axisymmetric) advective–diffusive flux-transport models to clarify to what extent the value of the magnetic diffusivity and its radial gradient influence such a difference. Moreover, we will study the role of the radial gradient of the latitudinal flow velocity.

2 MODELS AND METHODS

For the sake of simplicity, we consider the evolution of azimuthally averaged, purely poloidal, i.e., meridional fields. Quite generally, studying averaged fields requires the inclusion of an additional mean electromotive force \mathcal{E} in the induction equation. Its major constituents are often described by the α effect, turbulent pumping and turbulent diffusivity η_t (see e.g. Moffatt 1978). However, only the latter will be taken into account here and assumed to be isotropic, yet possibly depending on depth. We do not claim that all other turbulence effects, like dynamo waves or pumping, are negligible, but prefer to clarify the origin of the speed deviations in question by considering the effects in isolation. Thus, we focus here on the competition between diffusion and advection.

*E-mail: guerrero@nordita.org

¹ Local helioseismology inversions, e.g. ring diagram analysis (Haber et al. 2002) or time–distance helioseismology (Zhao & Kosovichev 2004; Zhao et al. 2011), in general tend to agree with the Doppler results.

Our model is kinematic and we consider axisymmetric solutions of the induction equation in spherical coordinates (r, θ, ϕ) :

$$\frac{\partial \mathbf{B}}{\partial t} = \nabla \times (\mathbf{U} \times \mathbf{B} - \eta_T \nabla \times \mathbf{B}), \quad \nabla \cdot \mathbf{B} = 0, \quad (1)$$

with the total (molecular plus turbulent) magnetic diffusivity $\eta_T = \eta + \eta_t$ and the *prescribed* velocity \mathbf{U} , i.e. we disregard the back-reaction of the magnetic field on to \mathbf{U} . The computational domain spans over a spherical half-shell $R_b \leq r \leq R$, $0 \leq \theta \leq \pi/2$ (i.e. from the pole to the equator), where R is the solar radius and the base of the convection zone is at $R_b = 0.7R$. The total diffusivity η_T is, unless specified otherwise, constant across the domain and considered a free parameter of the model.

For the one-dimensional version of the model, we solve the radial part of equation (1) for B_r at $r = R$, as done in several surface-transport models (see e.g. DeVore, Sheeley & Boris 1984; Baumann et al. 2004):

$$\frac{\partial B_r}{\partial t} = -\frac{1}{R \sin \theta} \frac{\partial}{\partial \theta} \left[\sin \theta \left(U_\theta B_r - \frac{\eta_T}{R} \frac{\partial B_r}{\partial \theta} \right) \right]. \quad (2)$$

Note that this equation is subject to the simplifying assumption $B_\theta \ll B_r$ at the surface (see the appendix of DeVore et al. 1984), the consequences of which will be assessed later when discussing our results. We solve equation (2) by using a second-order finite difference scheme with 512 grid points.² The time integration is performed with an implicit (Crank–Nicholson) method.

For the two-dimensional version, we solve instead of equation (1) the corresponding equation for the ϕ component of the vector potential $\mathbf{A} = A \hat{\phi}$, where $\mathbf{B} = \nabla \times \mathbf{A}$, and

$$\frac{\partial A}{\partial t} = -\frac{1}{s} (\mathbf{U} \cdot \nabla)(sA) + \eta_T \left(\nabla^2 - \frac{1}{s^2} \right) A, \quad s = r \sin \theta, \quad (3)$$

again utilizing finite differences (Lax–Wendroff scheme for first and centred second-order scheme for second derivatives). For all simulations we use 400^2 grid points. A convergence analysis revealed that for the global evolution of the magnetic field a resolution of 128^2 grid points is already sufficient. However, a smoother profile of the estimated tracer velocity is obtained with the higher resolution. Time integration is done with the alternating direction implicit method (for details see Guerrero & Muñoz 2004).

In modelling the meridional velocity \mathbf{U} , we start with the corresponding mass flow $\rho \mathbf{U}$ which is assumed steady and has thus to obey $\nabla \cdot (\rho \mathbf{U}) = 0$ because of mass conservation. Hence, it can be derived from a stream function ψ by $\rho \mathbf{U} = \nabla \times (\psi \hat{\phi})$. Following Dikpati et al. (2010), we assume an adiabatic density profile:

$$\rho(r) = \rho_0 (R/r - 0.97)^{1.5}, \quad (4)$$

where ρ_0 is specified such that $\rho(R) = 5 \times 10^{-3} \text{ g cm}^{-3}$. For the stream function, we choose the ansatz $\psi = -\psi_0 F(r) \partial_\theta G(\theta)$ with

$$F(r) = \left(\frac{R}{r} - 0.97 \right)^n \left[1 - \left(\frac{r}{R} \right)^k \right] \left[\left(\frac{R_b}{R} \right)^k - \left(\frac{r}{R} \right)^k \right], \quad (5)$$

$$G(\theta) = P_2(\cos \theta) + m P_4(\cos \theta), \quad (6)$$

where P_l is the Legendre polynomial of order l . $F(r)$ guarantees vanishing U_r at the boundaries $r = R_b, R$ assumed impenetrable. The first factor in $F(r)$, resembling the density profile, is necessary to avoid local extrema of U_θ within the domain. This can be achieved by $n = 0.8 \dots 1.2$, depending on the value of k . Apart from that, the exponents n and k are free parameters determining the steepness of

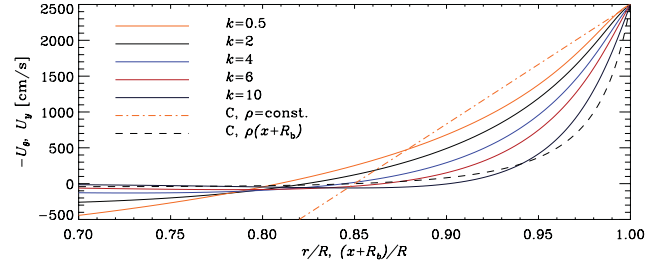


Figure 1. Solid lines: radial profile of $U_\theta(r, 57^\circ)$ for different k as indicated in the legend, $n = 0.8$, cf. equation (5). Broken lines: Cartesian velocity profile, $U_y(x, L_y/2)$, cf. equation (11).

the radial U_θ profile. For fixed n , lower (higher) values of k result in a flatter (steeper) profile (see Fig. 1).

Tuning the exponent n allows adjusting the U_θ gradient just at the surface without changing it very strongly deeper down. So n can be employed for ensuring the stress-free boundary condition $(\partial_r U_\theta)(R, \theta) = U_\theta(R, \theta)/R$, usually imposed in, e.g., mean-field hydrodynamic models of stellar rotation and in direct numerical simulations of convection. Here, it can be expressed in the form $h_r(R) = 1$, where $h_r(r)$ is the normalized radial gradient of U_θ , $h_r(r) = r(d \ln F/dr)$. For simplicity, we have ignored this condition in most of our calculations and fixed $n = 0.8$. However, we have checked the influence of having the stress-free condition obeyed on our results in a number of cases with different values of n .

Further, the choice of $m = -0.2$ results in a latitudinal surface profile $U_\theta(R, \theta)$ which resembles Doppler velocity observations (see e.g. Ulrich 2010), in particular the position of the surface maximum of $U_\theta(R, \theta)$ is fairly well reproduced. ψ_0 is adjusted such that this maximum is $U_0 = 2500 \text{ cm s}^{-1}$.

The initial magnetic field of a bipolar region is modelled as a flux loop in a meridional plane corresponding to two rings of concentrated magnetic flux on the surface of the sphere. We describe it by the vector potential

$$\mathbf{A} = A_0 \exp \left[-\left(\frac{\theta - \theta_i}{w_\theta} \right)^2 \right] \exp \left[-\left(\frac{r - R}{w_r} \right)^2 \right] \hat{\phi}, \quad (7)$$

where θ_i is the initial latitudinal location of the centre of the bipolar region. The initial separation between the positions at which B_r assumes its extrema at the surface, that is the ‘spot separation’, is $\gtrsim \sqrt{2} w_\theta$, whereas the depth to which the loop extends is controlled by w_r . We assume $w_\theta = 0.02$ (2.3°) and $w_r = 0.04R$ throughout this Letter. For the corresponding field geometry, see Fig. 2.

Magnetic boundary conditions are chosen to be consistent with a perfect conductor in $r \leq R_b$ and to ensure continuity of \mathbf{B} with

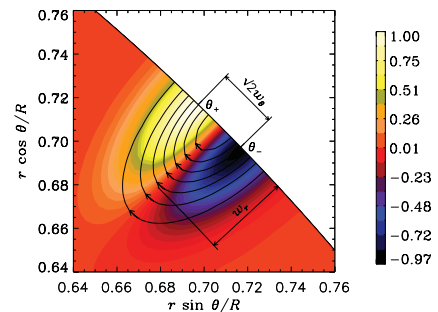


Figure 2. Bipolar region according to equation (7) for $\theta_i = 45^\circ$. θ_\pm is the position of the centre of the poleward (positive) and equatorward (negative) spot, respectively. Colour coding: $B_r/\max(B_r)$.

² Same results are obtained for resolutions from 128 to 1024 grid points.

an external potential field at $r = R$. Comparisons with the simpler normal field condition $\mathbf{r} \times \mathbf{B} = \mathbf{0}$ instead of the potential field condition showed no notable difference in the results. At the equator, \mathbf{B} is assumed to be antisymmetric.

Both models were run over the model time interval T , being typically two weeks, for 20 equidistant initial latitudes θ_i of the bipolar region between 5° and 85° . For measuring the latitudinal surface drift velocity of the flux loop, averaged over T , two different methods were employed. In the first one, the position θ_0 , at which the normal magnetic field B_r vanishes (i.e. the place where A peaks), was followed. In the second, we trace the positions of the local maximum and minimum of B_r within the loop, θ_+ and θ_- , respectively. The averaged latitudinal velocity was then defined as $\bar{V}_0 = R[\theta_0(T) - \theta_0(0)]/T$ in the first case and as the average of the two values $\bar{V}_\pm = R[\theta_\pm(T) - \theta_\pm(0)]/T$, that is

$$\bar{V} = (\bar{V}_+ + \bar{V}_-)/2, \quad (8)$$

in the second. We assign \bar{V}_0 to the average colatitude $[\theta_0(T) + \theta_0(0)]/2$, but \bar{V} to the average $[\theta_+(T) + \theta_-(T) + \theta_+(0) + \theta_-(0)]/4$. As the profiles $\bar{V}(\theta)$ and $\bar{V}_0(\theta)$, obtained directly in this way, turned out to be rather wiggly, we assumed for simplicity that a reasonably smooth fitting function is given by $\hat{V}G(\theta)$ (see equation 6), with the amplitude \hat{V} as single fit parameter. That is, we assumed that the tracking velocity \bar{V} has (up to some factor) the same θ dependence as the flow speed at the surface, $U_\theta(R, \theta)$. For the highest diffusivity used and for starting latitudes θ_i closest to the equator, the influence of this reflecting boundary becomes notable. This influence leads to an unrealistically low velocity of the equatorward (negative) spot which, in turn, corrupts \bar{V} . We use instead \bar{V}_0 there.

3 RESULTS

3.1 One-dimensional model

In simulations with high diffusivity, $\eta_T = 10^{12} \text{ cm}^2 \text{ s}^{-1}$, we find that the speed of the poleward (equatorward) spot, $\bar{V}_+(\bar{V}_-)$, is larger (smaller) than the fluid velocity (see Fig. 3). However, the average velocity \bar{V} matches the fluid velocity U_θ fairly well. The velocity of the centre of the bipolar region, \bar{V}_0 , also coincides with it. For even higher values of η_T , \bar{V}_+ and \bar{V}_- deviate stronger from U_θ , but the average continues to agree with it. For evolution times shorter than two weeks (e.g. one week or less), the curve for \bar{V} is more wiggly. However, it always follows the flow. These results agree with those of the two-dimensional (θ, ϕ) model of Wang et al. (2009), where

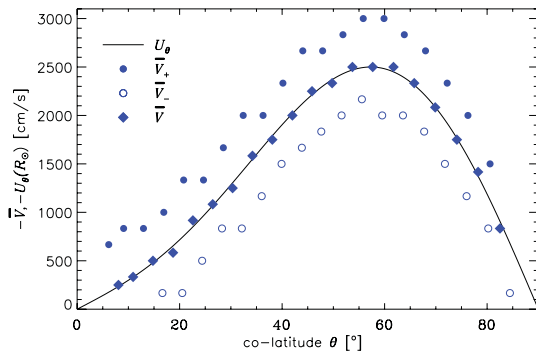


Figure 3. Tracking velocities for the one-dimensional model equation (2) with $\eta_T = 10^{12} \text{ cm}^2 \text{ s}^{-1}$. Solid line: flow velocity $U_\theta(R)$; filled and open circles: \bar{V}_+ and \bar{V}_- , respectively; diamonds: average $\bar{V} = (\bar{V}_+ + \bar{V}_-)/2$.

the poleward spots of the bipolar regions move faster than the fluid for a similar value of η_T (see their fig.15).

3.2 Two-dimensional model

Next, we study the evolution of a two-dimensional bipolar region by solving equation (3) using equation (7) as initial condition. As a representative case, Fig. 4 shows the evolution of a bipolar region initially located at $\theta_i = 45^\circ$, using $k = 6$ with either $\eta_T = 10^9$ (left) or $10^{12} \text{ cm}^2 \text{ s}^{-1}$ (right).

In contrast to the one-dimensional model, where the profile $\bar{V}(\theta)$ turns out to be independent of η_T , we find here a significant dependence. For small values of η_T , the ‘frozen-in’ condition is fulfilled and thus the magnetic field lines appear indeed attached to the plasma flow. (The systematic offset between \bar{V} and U_θ for $\eta_T \rightarrow 0$, visible in Figs 5 and 6, is mainly due to the discretization errors.) For larger η_T ($\gtrsim 3 \times 10^{11} \text{ cm}^2 \text{ s}^{-1}$), however, the diffusion time-scale becomes similar to or even smaller than the advection time-scale, and then there is an increasing departure from the ‘frozen-in’ state. This becomes clear in Fig. 5, where $\bar{V}(\theta)$ is shown for $10^8 \leq \eta_T \leq 3 \times 10^{12} \text{ cm}^2 \text{ s}^{-1}$. In general, its deviation from U_θ increases everywhere with growing η_T , while for each η_T it adopts its largest value at intermediate latitudes of $\approx 57^\circ$ where U_θ peaks. Note that the simple fit based only on the amplitude, using the function G from equation (6), works remarkably well.

The top panel of Fig. 6 visualizes the dependence of \bar{V} on the radial variation of U_θ , i. e. on the index k in equation (6). We present \bar{V} at the latitude where U_θ peaks ($\theta \approx 57^\circ$) as a function of

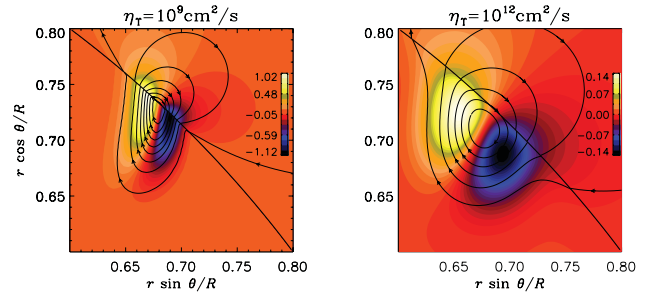


Figure 4. Magnetic field (solid lines) after two weeks of evolution of a bipolar region initially at $\theta_i = 45^\circ$ (see Fig. 2). Colour coding: $B_r/\max[B_r(t=0)]$. Left: $\eta_T = 10^9 \text{ cm}^2 \text{ s}^{-1}$; right: $\eta_T = 10^{12} \text{ cm}^2 \text{ s}^{-1}$.

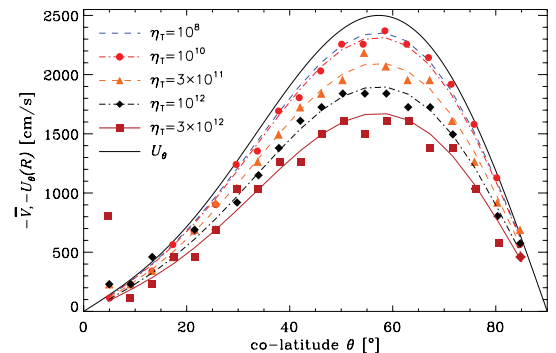


Figure 5. Tracking velocity $\bar{V}(\theta)$ for $10^8 \leq \eta_T \leq 3 \times 10^{12} \text{ cm}^2 \text{ s}^{-1}$, $k = 6$. Solid/black: flow velocity $U_\theta(R, \theta)$. Symbols: \bar{V} according to equation (8), omitted for $\eta_T = 10^8 \text{ cm}^2 \text{ s}^{-1}$ as mostly coinciding with those for $\eta_T = 10^{10} \text{ cm}^2 \text{ s}^{-1}$; symbol for $\eta_T = 3 \times 10^{12} \text{ cm}^2 \text{ s}^{-1}$, $\theta = 85^\circ$ shows \bar{V}_0 . Lines: fit to G in equation (6) with amplitude as fit parameter, $m = -0.2$ fixed. Colours/symbols/line styles correspond to different η_T according to legend.

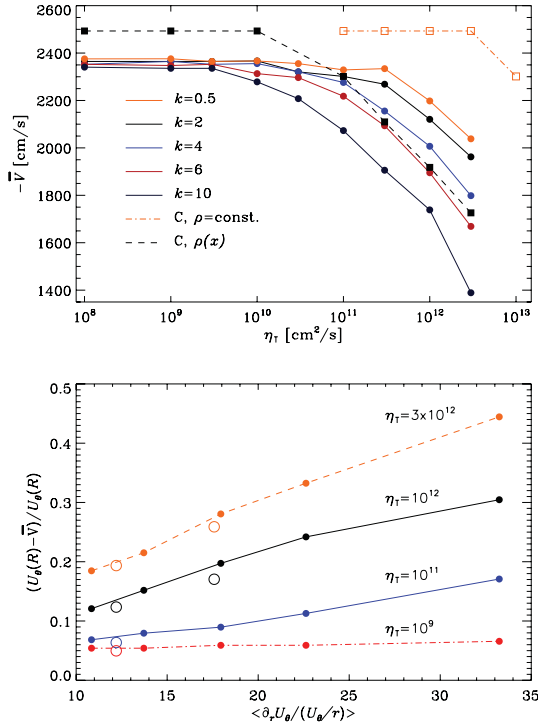


Figure 6. Upper panel: maximum tracking velocity \bar{V} versus η_T for different values of k in equation (6). Solid lines/filled circles correspond to the spherical model (values taken from fit curves). Broken lines/squares correspond to the Cartesian model (C); dashed/filled squares: density according to equation (4), dot-dashed/open squares: constant density. Lower panel, lines/closed circles: fractional speed difference, $[U_\theta(R) - \bar{V}]/U_\theta(R)$, versus the normalized radial gradient of U_θ , $h_r(r)$, averaged over $r/R = 0.97 \dots 1$. Open circles: stress-free boundary condition ensured in the profile (5) by $(n, k) = (0.954, 4)$ for $\langle h_r \rangle \approx 12$ and $(1.194, 10)$ for $\langle h_r \rangle \approx 17.5$.

η_T for k varying from 0.5 to 10. To minimize the effect of numerical noise, we have taken \bar{V} from fit curves. For $k = 0.5$ (yellow line), \bar{V} does not depend on η_T up to $10^{11} \text{ cm}^2 \text{ s}^{-1}$. Beyond this value, \bar{V} starts to decrease. For increasing k the curves depart from the ‘frozen-in’ domain at decreasing values of η_T being as small as $\approx 3 \times 10^9 \text{ cm}^2 \text{ s}^{-1}$ for $k = 10$. The bottom panel of the same figure shows the fractional velocity difference, $[U_\theta(R) - \bar{V}]/U_\theta(R)$, again taken at $\theta = 57^\circ$, as a function of the normalized radial gradient of U_θ , $h_r(r)$, averaged over the interval $r = 0.97R, \dots, R$, where the major part of the magnetic flux is residing. Note that for the highest diffusivity, $3 \times 10^{12} \text{ cm}^2 \text{ s}^{-1}$, \bar{V} is reduced by ≈ 45 per cent at $\langle h_r \rangle \approx 33$. Employing our results for interpreting the data given in fig. 10 of Ulrich (2010), we find that their speed reductions of about 30 per cent do occur in our model, either for $\eta_T = 3 \times 10^{12} \text{ cm}^2 \text{ s}^{-1}$ and $\langle h_r \rangle \approx 20$ or for $\eta_T = 10^{12} \text{ cm}^2 \text{ s}^{-1}$ and $\langle h_r \rangle \approx 33$. In the bottom panel of Fig. 6, some results are shown with the profile (5) adjusted to the stress-free boundary condition by fine tuning of n . Obviously, there is only a slight reduction of the velocity difference in comparison with the unadjusted profile.

3.3 Dependency on $\eta_T(r)$

Having examined the influence of the radial profile of U_θ on \bar{V} , one must ask whether also the radial profile of η_T has an effect. However, abandoning the assumption of its constancy, that is, of the homogeneity of the turbulence behind it, isotropy becomes questionable, too. We postpone the inclusion of anisotropy until reliable data for

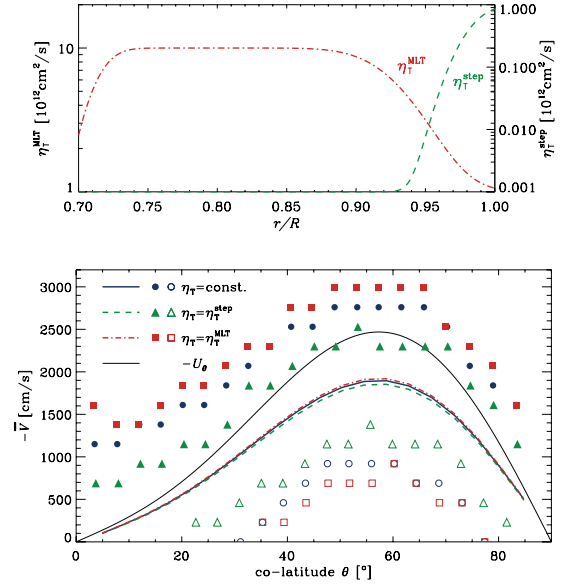


Figure 7. Top: profiles of η_T used. Bottom: corresponding tracking velocities \bar{V} for $\eta_T(R) = 10^{12} \text{ cm}^2 \text{ s}^{-1}$, $k = 6$. Coloured lines: fits to equation (6). Solid/black: flow velocity $U_\theta(R)$. Filled (open) symbols: \bar{V}_+ (\bar{V}_-).

the tensor describing the part $\eta_{ijk} \partial_k B_j$ of the mean electromotive force, say, from convection simulations and the test-field method (see e.g. Käpylä, Korpi & Brandenburg 2009) are available.

From an observational point of view, the η_T profile is unknown. Hence, the profiles so far considered in dynamo models are to some extent arbitrary. For instance, Dikpati & Gilman (2001) and Guerrero & de Gouveia Dal Pino (2007) have used a step function, with values of $10^{10} \text{ cm}^2 \text{ s}^{-1}$ in the bulk of the convection zone and $\approx 10^{12} \text{ cm}^2 \text{ s}^{-1}$ for supergranular diffusion within the so-called near-surface shear layer. On the other hand, Pipin et al. (2011) considered a mixing length theory (MLT) estimate of η_t . Here we consider both a step and an MLT profile defined by the following expressions (see the top panel of Fig. 7):

$$\eta_T^{\text{step}} = \eta_{cz} + \frac{\eta_s - \eta_{cz}}{2} \left[1 + \text{erf} \left(\frac{r - 0.96R}{0.02R} \right) \right], \quad (9)$$

with $\eta_s = 10^{12} \text{ cm}^2 \text{ s}^{-1}$ and $\eta_{cz} = 10^{-2} \eta_s$, and

$$\eta_T^{\text{MLT}} = \eta_{rz} + \frac{\eta_{cz} - \eta_{rz}}{2} \left[1 + \text{erf} \left(\frac{r - 0.71R}{0.02R} \right) \right] + \frac{\eta_s - \eta_{cz}}{2} \left[1 - \text{erf} \left(\frac{r - 0.93R}{0.04R} \right) \right], \quad (10)$$

where $\eta_{rz} = 10^8 \text{ cm}^2 \text{ s}^{-1}$, $\eta_s = 10^{13} \text{ cm}^2 \text{ s}^{-1}$ and $\eta_{cz} = 10^{-1} \eta_s$.

We have performed numerical experiments with $k = 6$ for U_θ and a fixed surface value $\eta_T(R) = 10^{12} \text{ cm}^2 \text{ s}^{-1}$. The results, displayed in the bottom panel of Fig. 7, do not show marked differences between the three diffusivity profiles considered, and the fitted MFT velocity profiles are nearly identical with that for $\eta = \text{constant}$. However, the separation between poleward and equatorward spots is smaller for the model with the step profile. The model with constant η_T exhibits an intermediate separation, whereas in the model with the MLT profile the dispersion increases.

3.4 Comparison with Cartesian geometry

To assess the influence of the curvature in our spherical model, we have repeated some of the simulations in a two-dimensional

$(L_x \times L_y)$ Cartesian box with aspect ratio $(R - R_b) : R \pi/2$ and the simplified circulation velocity,

$$\mathbf{U} = \frac{1}{\rho} \nabla \times (\psi \hat{\mathbf{e}}_z), \quad \psi = \psi_0 \frac{x}{L_x} \left(\frac{x}{L_x} - 1 \right) \frac{y}{L_y} \left(\frac{y}{L_y} - 1 \right), \quad (11)$$

with (x, y) corresponding to (r, θ) , respectively, ρ set either constant or to $\rho(x + R_b)$ from equation (4), and ψ_0 again adjusted to yield 2500 cm s^{-1} for the maximum surface velocity. Instead of the vacuum boundary condition at $r = R$, the simpler normal field condition $\hat{\mathbf{e}}_x \times \mathbf{B} = \mathbf{0}$ was imposed at $x = L_x$. These simulations were performed with the PENCIL CODE,³ which uses sixth-order explicit finite differences in space and third-order accurate time stepping method. For these runs we use 512^2 grid points.

The results, here with constant η_T , for both choices of ρ , are represented by broken lines in Fig. 6. The corresponding profiles $U_y(x, L_y/2)$ are shown in Fig. 1 with the same line styles. Clearly, these findings agree with those of the spherical model, showing that the value of η_T , at which the frozen-in condition starts to fail, depends crucially on the radial (x) gradient of U_y and varies here by about two orders of magnitude.

4 DISCUSSION AND CONCLUSIONS

Through one- and two-dimensional advective–diffusive models, we have investigated the differences between the surface meridional flow speed obtained from Doppler measurements and that inferred from MFT. In the one-dimensional simulations, the average velocity of the magnetic tracers always coincides with that of the flow, independently of the value of η_T . In the two-dimensional models, on the other hand, flow and feature-tracking velocities may diverge at higher diffusivities, for which the ‘frozen-in’ condition does no longer hold. Further, the difference between these velocities depends on the radial gradient of the latitudinal velocity: the steeper the profile U_θ , the larger the difference. Using a different code, we have verified that these results apply also in Cartesian geometry. To understand this dependence, we refer to the induction equation (for simplicity in Cartesian coordinates), taken at the surface $x = L_x$ (or $r = R$), where $U_x = \partial_y U_x = 0$, so

$$\frac{\partial B_x}{\partial t} = -\frac{\partial}{\partial y}(U_y B_x) + \eta_T \left(\frac{\partial^2 B_x}{\partial x^2} + \frac{\partial^2 B_x}{\partial y^2} \right), \quad (12)$$

$$\frac{\partial B_y}{\partial t} = \frac{\partial}{\partial x}(U_y B_x - U_x B_y) + \eta_T \left(\frac{\partial^2 B_y}{\partial x^2} + \frac{\partial^2 B_y}{\partial y^2} \right). \quad (13)$$

Note that B_x is apparently decoupled from B_y , but at the price of being coupled to its second vertical derivative. In the case of small η_T (i.e. diffusion time larger than advection time), the evolution of B_x is governed by the first, advective, term in equation (12). In this case, the magnetic field lines follow the fluid velocity locally (see curved magnetic field lines in the left-hand panel of Fig. 4). In the case of larger η_T (diffusion time similar to or shorter than advection time), the diffusion term in equation (12) plays a significant role in the field evolution. The dependence on $\partial_x^2 B_x$ can be eliminated by

the solenoidal condition $\partial_x B_x + \partial_y B_y = 0$, by which the coupling between the two equations becomes obvious. Because B_y depends explicitly on $\partial_x U_y$, the surface speed of B_x will clearly be modified by the fluid motion deeper down in the subsurface layers. When ignoring B_y from the beginning, however, as done in DeVore et al. (1984), and many surface-transport models afterwards, this influence will be lost. In spherical coordinates, the surface induction equation for B_r exhibits an analogous dependence on B_θ , hence the same argument is valid.

Based upon our results for the difference between flow and MFT speeds, one might think of inferring the thickness of the layer where the flow is polewards. This value, however, would depend on the surface diffusivity and on $\partial_r U_\theta$, both of which are poorly known. Hathaway (2011) has inferred an extreme flow pattern with a very shallow poleward flow ($\approx 35 \text{ Mm}$ deep) which nevertheless can be brought into agreement with our findings, requiring a large radial gradient of U_θ , $\langle h_r(r) \rangle \gtrsim 20$ (cf. Fig. 6). Furthermore, surface flux-transport models in two dimensions (θ, ϕ), which disregard the radial derivatives in B_r , are probably overestimating the importance of advection in their results.

ACKNOWLEDGMENTS

The authors thank the anonymous referee for her/his valuable comments. This work started during the NORDITA programme on predictability and data assimilation and is supported by the European Research Council under the AstroDyn research project 227952. MD thanks the support by NASA’s Living With a Star programme through the grant NNX08AQ34G.

REFERENCES

- Baumann I., Schmitt D., Schüssler M., Solanki S. K., 2004, *A&A*, 426, 1075
 DeVore C. R., Sheeley, N. R., Jr, Boris J. P., 1984, *Sol. Phys.*, 92, 1
 Dikpati M., Gilman P. A., 2001, *ApJ*, 559, 428
 Dikpati M., Gilman P. A., Ulrich R. K., 2010, *ApJ*, 722, 774
 Guerrero G., de Gouveia Dal Pino E. M., 2007, *A&A*, 464, 341
 Guerrero G. A., Muñoz J. D., 2004, *MNRAS*, 350, 317
 Haber D. A., Hindman B. W., Toomre J., Bogart R. S., Larsen R. M., Hill F., 2002, *ApJ*, 570, 855
 Hathaway D. H., 2011, preprint (arXiv:1103.1561)
 Hathaway D. H., Rightmire L., 2010, *Sci*, 327, 1350
 Käpylä P. J., Korpi M. J., Brandenburg A., 2009, *A&A*, 500, 633
 Komm R. W., Howard R. F., Harvey J. W., 1993, *Sol. Phys.*, 147, 207
 Moffatt H. K., 1978, *Magnetic Field Generation in Electrically Conducting Fluids*. Cambridge Univ. Press, Cambridge
 Pipin V. V., Kuzanyan K. M., Zhang H., Kosovichev A. G., 2011, preprint (arXiv:1105.4285)
 Sheeley, N. R., Jr, 2010, in Cranmer S. R., Hoeksema J. T., Kohl J. L., eds, *ASP Conf. Ser. Vol. 428, SOHO-23: Understanding a Peculiar Solar Minimum*. Astron. Soc. Pac, San Francisco, p. 3
 Ulrich R. K., 2010, *ApJ*, 725, 658
 Wang Y.-M., Robbrecht E., Sheeley N. R., 2009, *ApJ*, 707, 1372
 Zhao J., Kosovichev A. G., 2004, *ApJ*, 603, 776
 Zhao J. et al., 2011, *Sol. Phys.*, doi:10.1007/s11207-011-9757-y

³ <http://pencil-code.googlecode.com/>

This paper has been typeset from a \LaTeX file prepared by the author.